Reconstruction and modeling of 3D percolation networks of carbon fillers in a polymer matrix

Author's version
Published in
International Journal of Thermal Sciences 49(12), pp 2272/2281
DOI: 10.1016/j.ijthermalsci.2010.07.019
http://dx.doi.org/10.1016/j.ijthermalsci.2010.07.019

Reconstruction and modeling of 3D percolation networks of carbon fillers in a polymer matrix

Eliodoro Chiavazzo
Politecnico di Torino, Corso Duca degli Abruzzi 24, 10129 Torino Italy,
eliodoro.chiavazzo@polito.it

Pietro Asinari
Politecnico di Torino, Corso Duca degli Abruzzi 24, 10129 Torino Italy,
pietro.asinari@polito.it

Abstract

In the present work, we illustrate a methodology for the reconstruction and modeling of three-dimensional micro-structures of highly anisotropic composite materials. Specifically, we focus on disk-shaped nano-fillers dispersed in a polymer matrix and detailed numerical investigations, based on the lattice Boltzmann method (LBM), are carried out on the global thermal conductivity.

Key Words: *Lattice Boltzmann method, Thermal conductivity, Carbon nano-fillers, Continuum percolation theory.*

Symbols [1]

PP	Polypropylene	[–]
KS4	Commercial graphite	[–]
LB	Lattice Boltzmann	[–]
SEM	Scanning electron microscope	[–]
S	Generic surface	[–]
A	Area of a surface	[μm^2]
x, y, z	Cartesian axes	[–]
Q	Global rate of conductive heat	[LB]
Q_f	Rate of conductive heat through the filler	[LB]

[1] According to the standard lattice Boltzmann method, all the physical quantities involved are dimensionless: In the nomenclature, this is indicated by the notation [LB].

Q_p	Rate of conductive heat through the polymer matrix	[LB]
k_f, k_f^p	Thermal conductivity of the filler	[LB]
k_p	Thermal conductivity of the polymer	[LB]
k_{eff}	Global thermal conductivity	[LB]
T	Temperature	[LB]
T_f	Temperature of filler	[LB]
T_p	Temperature of polymer matrix	[LB]
∂_γ	Partial derivative with respect to γ	[$-$]
p_f	Volume fraction of the filler	[$-$]
Y_f	Mass fraction of the filler	[$-$]
ρ_f	Mass density of the filler	[$\mathrm{g \cdot cm^{-3}}$]
ρ_p	Mass density of the polymer	[$\mathrm{g \cdot cm^{-3}}$]
p	Volume (Area) fraction	[$-$]
p_c	Percolation threshold	[$-$]
n	Particle concentration per unit volume (area)	[$\mathrm{m^{-3}(m^{-2})}$]
n_c	Critical particle concentration per unit volume (area)	[$\mathrm{m^{-3}(m^{-2})}$]
L	Box edge	[$\mu\mathrm{m}$]
a, b, c	Semi-axes of ellipses and ellipsoids	[$\mu\mathrm{m}$]
ε	Aspect ratio	[$-$]
η	Cumulative volume of spheres in the unit box	[$-$]
η_c	Critical cumulative volume of spheres per unit volume	[$-$]
ϕ	Particle size	[$\mu\mathrm{m}$]
ϕ_{min}	Smallest particle size	[$\mu\mathrm{m}$]
ϕ'	Shifted particle size	[$\mu\mathrm{m}$]
D_{10}, D_{50}, D_{90}	Diameters	[$\mu\mathrm{m}$]
f	Distribution function of particle size	[$\mu\mathrm{m^{-1}}$]
F	Cumulative curve of f	[$-$]
$\bar{\alpha}$	Dimensionless parameter of f	[$-$]

$\bar{\beta}$	Parameter of f	[$\mu\mathrm{m}^{-(1+\bar{\alpha})}$]
$\bar{\mu}$	Parameter of f	[$\mu\mathrm{m}$]
$\bar{\sigma}$	Parameter of f	[$\mu\mathrm{m}$]
R	Rotation matrix	[$-$]
R_x	Rotation matrix of x-axis	[$-$]
R_y	Rotation matrix of y-axis	[$-$]
R_z	Rotation matrix of z-axis	[$-$]
$\vartheta_x, \vartheta_y, \vartheta_z$	Rotation angles	[rad]
$\bar{\vartheta}_x, \bar{\vartheta}_y$	Mean rotation angles	[rad]
σ	Variance	[rad]
N	Number of lattice nodes along each Cartesian axis	[$-$]
dx	Spacial stepping along x-axis	[$\mu\mathrm{m}$]
dy	Spacial stepping along y-axis	[$\mu\mathrm{m}$]
dz	Spacial stepping along z-axis	[$\mu\mathrm{m}$]
V_c	Cumulative volume of particles in the unit box	[$-$]
$\mathcal{M}$	Mesh array	[$-$]
$\mathcal{A}, \mathcal{B}$	Box facets	[$-$]
$(T_h - T_c)$	Temperature difference between $\mathcal{A}$ and $\mathcal{B}$	[LB]
l	Line connecting $\mathcal{A}$ and $\mathcal{B}$	[$-$]
$D3Q19$	Lattice Boltzmann scheme	[$-$]
f_i	Lattice Boltzmann populations	[LB]
f_i^{eq}	Lattice Boltzmann equilibrium populations	[LB]
$\vec{c}_i = (c_{ix}, c_{iy}, c_{iz})$	Velocities of the lattice Boltzmann populations	[LB]
ω	Relaxation frequency	[LB]
ω_f	Relaxation frequency of filler	[LB]
ω_p	Relaxation frequency of polymer matrix	[LB]
$\boldsymbol{x}$	Arbitrary point of the computational domain	[LB]
t	Time	[LB]

dt	Time stepping	[LB]
w_i	weight of the i-th population	[$-$]
$\vec{j} = (j_x, j_y, j_z)$	First order moment	[LB]
c_s^2	Parameter	[LB]
ρ	Mass density	[LB]
c_p	Specific heat capacity	[LB]
α	Thermal diffusivity	[LB]
∇T	Temperature gradient	[LB]
∇T_f	Temperature gradient of filler	[LB]
∇T_p	Temperature gradient of polymer matrix	[LB]
$\hat{n}$	Unit normal vector	[$-$]
S_i	Random configuration of a composite material sample	[$-$]
R_x^2, R_z^2	Coefficients of determination	[$-$]
θ	Angle of the orientation of the extrusion axis	[rad]
i, β, γ, τ	indexes	[$-$]

1. Introduction and motivation

A large variety of additives are nowadays available to endow polymer compounds with enhanced physical properties, such as transport quantities (electrical and thermal conductivity) and elastic moduli. Due to the recent development of novel carbon-based particles with excellent properties, composite materials showing high performances are expected. The present work describes a general numerical tool aiming at characterizing the global thermal conductivity of percolating networks of highly conductive nano-fillers, dispersed in a polymer matrix: In particular, here we focus on extruded composite material made of polypropylene and graphite nano-particles. Starting from two-dimensional scanning electron microscope (SEM) images, the micro-topology of material samples is reconstructed, discretized by means of a regular Cartesian mesh, and utilized for solving the unsteady heat conduction problem. Numerical simulations are based on a fully parallelized three-dimensional lattice Boltzmann (LB) solver, the computational domain is represented by a cube with a fixed temperature difference between two opposite facets, while periodic condition is assumed for the rest of the boundary. Since the computational effort is already demanding (meshes made of up-to 14 millions of points are considered), periodic boundary conditions allow one to increase the statistical reliability of the simulated sample ($L^3 = (15\mu m)^3$, which is statistically significant for catching

the main microscopic features of the considered heterogeneous materials). Since it is difficult to reconstruct topologies, made of randomly placed fillers, which are exactly periodic, the periodicity will be numerically forced: the effects of the resulting approximation can be included in the stochastic noise due to the reconstruction process and they will be checked by properly repeated numerical simulations.

General aspects on physical properties (such as thermal and electrical conductivity, mechanical properties, etc.) of composite materials can be investigated in the framework of the continuum percolation theory [1], as testified by the extensive literature in this field (see, e.g., [2, 3, 4, 5, 6, 7]). Notice that, the latter theory usually addresses the issue of evaluating the minimal fraction of filler that gives rise to a percolating network, under the assumption of randomly oriented particles of the same shape and size: Toward this end, the Monte Carlo Method is a typical numerical tool for such investigations [8].

However, the study of realistic composite materials often involves fillers with high aspect-ratio (e.g., tubes and lamellae) and significant differences in size. In addition, the hypothesis of fully random orientation may break down, if particles show a tendency to align along preferential lines or planes: This is, for example, the case of manufacturing by extrusion, where particles preferably align along the extrusion axis. As a matter of fact, performances of realistic composite materials, in terms of heat conduction, cannot be investigated only on the basis of the continuum percolation theory, and accurate numerical simulations become necessary (see also [10]).

This manuscript is organized in sections as follows. In section 2, the ideal upper limit of thermal conductivity of composite materials is discussed, while some basic notions on the continuum percolation theory are reviewed in section 3. In section 4, a methodology for the reconstruction of a composite material micro-topology is worked out. The mathematical model adopted for the evaluation of the global thermal conductivity of a composite material is discussed in section 5, while validation results are reported in section 6 for thermal resistances connected in series and parallel arrangements. Finally, results of numerical simulations of the global thermal conductivity are presented in section 7, and discussed in section 8.

2. Ideal limit

The most effective way to enhance thermal conductivity of a polymer, by mixing it with a highly conductive filler, is schematically represented in Fig. 1. In this ideal scenario, the amount of filler is fully exploited for generating percolating paths (with constant cross sectional area) throughout the poorly conductive matrix. At the steady state, the heat flux through a surface S with area A, orthogonal to $z-$ axis, is given by the Fourier's law:

$$Q = Q_f + Q_p = k_f p_f A \partial_z T + k_p (1 - p_f) A \partial_z T = \left[k_f p_f + k_p \left(1 - p_f\right)\right] A \partial_z T, \qquad (1)$$

where Q_f and Q_p denote the rate of conductive heat due to the filler and the polymer, respectively, while $\partial_z T$ is the derivative of temperature with respect to z. The global thermal conductivity of the composite material k_{eff} can be easily related to the thermal conductivity of filler k_f and polymer k_p as follows:

$$k_{eff} = \frac{Y_f}{\rho_f - Y_f\left(\rho_f - \rho_p\right)} k_f + \left(1 - \frac{Y_f}{\rho_f - Y_f\left(\rho_f - \rho_p\right)} \rho_p\right) k_p, \tag{2}$$

where ρ_p represents the density of the polymer, while ρ_f and Y_f are the density and the mass fraction of the filler, respectively. Based on formula (2), Fig. 2 shows that, in the ideal case, a small amount of filler is able to produce an increase in the thermal conductivity of the composite material k_{eff} up to a few orders of magnitude compared to k_p.

Nevertheless, instead of segregating as above, filler particles typically tend to randomly disperse within the polymer matrix. In this case, heat flow is delegated to both the polymer matrix and to highly non-regular percolating clusters of particles, which are created if a critical amount of filler is used. Notice that, now part of the filler is not exploited for conduction, and the value (2) only represents an ideal upper limit of k_{eff}. To some extent, this phenomenon can be investigated in the framework of the continuum percolation theory (e.g. the minimal amount of filler that gives rise to topologically connected paths throughout a composite material), however quantitative results require detailed numerical simulations, as describes in the sections below.

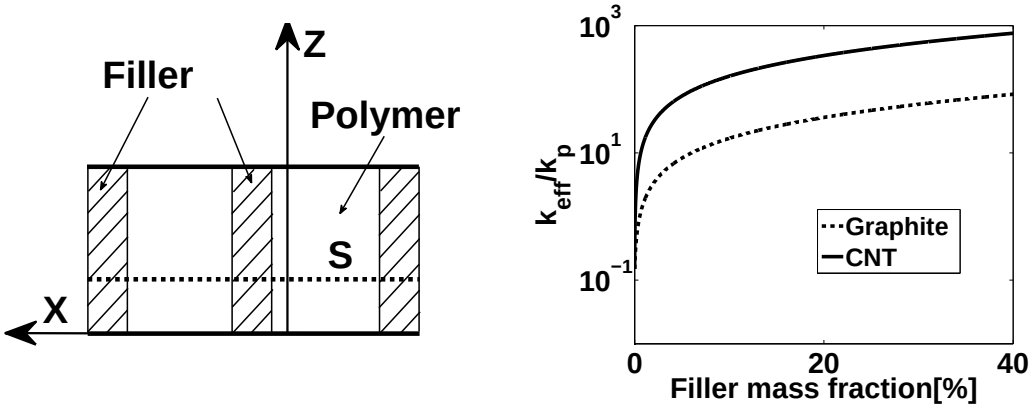

Figure 1: Left-hand side: Cross-section of an ideal composite material, where highest global thermal conductivity (along $z-$axis) k_{eff} is achieved with a fixed amount of filler. In principle, a small amount of filler is able to significantly increase the value of k_{eff}. Right-hand side: Here, we compare the benefit due to graphite (KS4) and carbon nano-tubes (CNT), where $k_{KS4} = 400[W/mK]$, $k_{CNT} = 3000[W/mK]$, $\rho_{KS4} = 1.75[g/cm^3]$ and $\rho_{KS4} = 2.255[g/cm^3]$ are assumed.

3. Continuum percolation theory

Below, we briefly review some basic notions of the continuum percolation theory, which will prove useful for a better understanding of this work. The interested reader can refer to classical

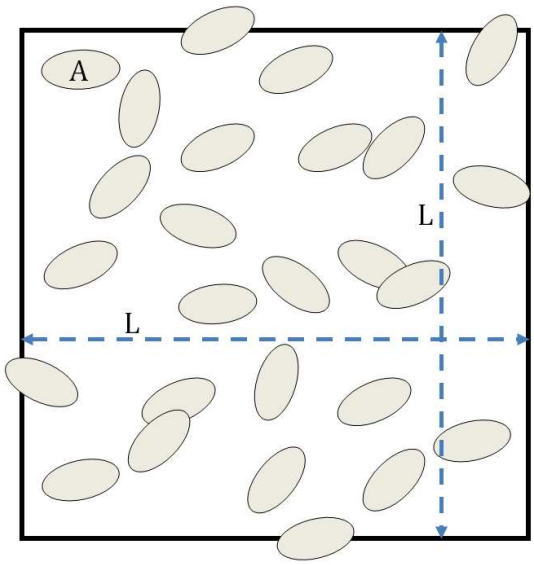

Figure 2: (Color online) Two dimensional model of a binary mixture: Identical ellipses with area A randomly dispersed in a square box with area $L \times L$.

works on percolation for further details (see, e.g., [1]).

General phenomena, where at least one pathway spans the entire domain of a physical system, can be described in the framework of percolation theory: In particular, transport and mechanical properties of multiphase compounds can be studied by referring to the continuum percolation theory [1, 2, 4]. Here, neglecting every detailed description of the interface contact among different phases, one is typically interested in evaluating the geometric percolation threshold p_c, namely the minimum amount of materials which gives rise to percolation. Percolation thresholds are indeed among the most important inputs in design and optimization of such materials. A two dimensional problem of continuum percolation theory is schematically illustrated in Fig. 2, where identical elliptical particles are randomly placed in a square box. Let p denote the fractional area of the white phase, namely the area of the box remaining after placing all the ellipses, whereas their fractional area is $1 - p$. It often proves convenient to relate fractional areas to particle concentrations per unit area n, because the latter only requires counting, and no area evaluation is involved. Under the assumption of sufficient randomness and identical particles, it is easy to find such a relation for any dimension and particle shape. In a configuration characterized by the concentration n (and fraction p), the area in the box free to be occupied by particles is pL^2. Hence, additional ellipses will remove the area pL^2Adn, while the concentration n increases up to $n + dn$ and A is the area of a single particle. Moreover, the free area in the box is reduced according to:

$$pL^2 - (p + dp)\, L^2 = pL^2Adn, \tag{3}$$

which can be recast as follows:

$$dp/p = -Adn, \tag{4}$$

i.e.,

$$p = e^{-An}. \tag{5}$$

Notice that, the generalization of (5) in three dimensions is straightforward, by replacing A with the particle volume. In the case of ellipses: $A = \pi ab$, with a and b denoting major and minor semiaxes, respectively. At percolation $n = n_c$, and the threshold can be computed as follows:

$$1 - p_c = 1 - e^{-\pi abn_c}. \tag{6}$$

For circles $a = b$, it is know from the literature [4] that

$$1 - p_c = 1 - e^{-\pi a^2 n_c} \simeq 0.67. \tag{7}$$

On the other hand, it has been observed that shape significantly affects the value of p_c, and particles with higher aspect ratio percolate at lower fractions [3]. For instance, in the *needle limit* where the ratio $b/a \ll 1$, the percolation threshold is [4]

$$1 - p_c \simeq 4.2b/a, \tag{8}$$

meaning that the smaller b/a the fewer needles cross the entire domain, and these have basically no area given that $p_c \to 1$.

In the following, we focus on binary mixtures of polypropylene and graphite particles (see Fig. 3 below) that we assume can be modeled as disk-shaped plates. Hence, for our purposes, here we are particularly interested in three dimensional systems, where ellipsoids of revolution are randomly placed in a matrix. Let a, b and c be three semiaxes of an arbitrary ellipsoid. Garboczi et al. [11] have investigated the influence of object shape on the percolation threshold p_c ranging from the extreme *prolate limit* ($a = b \ll c$) of needle-like particles to the extreme *oblate limit* ($a = b \gg c$) of plate-like particles. By means of asymptotic analysis, in the latter case, it has been found that:

$$1 - p_c = 1 - e^{-\eta_c \varepsilon}, \quad \eta_c = 1.27, \tag{9}$$

where the small parameters $\varepsilon = c/a = c/b$ defines the aspect ratio, while η is the volume of a sphere with radius $r = a = b$, multiplied by the particle concentration n:

$$\eta = \frac{4}{3}\pi a^3 n. \tag{10}$$

Notice that, more recent results show remarkable deviations from the result in (9) [8, 12]. For instance, based on Monte Carlo simulations, Yi et al [8] have found that $\eta_c = 0.9614$. The origin of such a discrepancy is not yet clear.

4. Micro-topology reconstruction

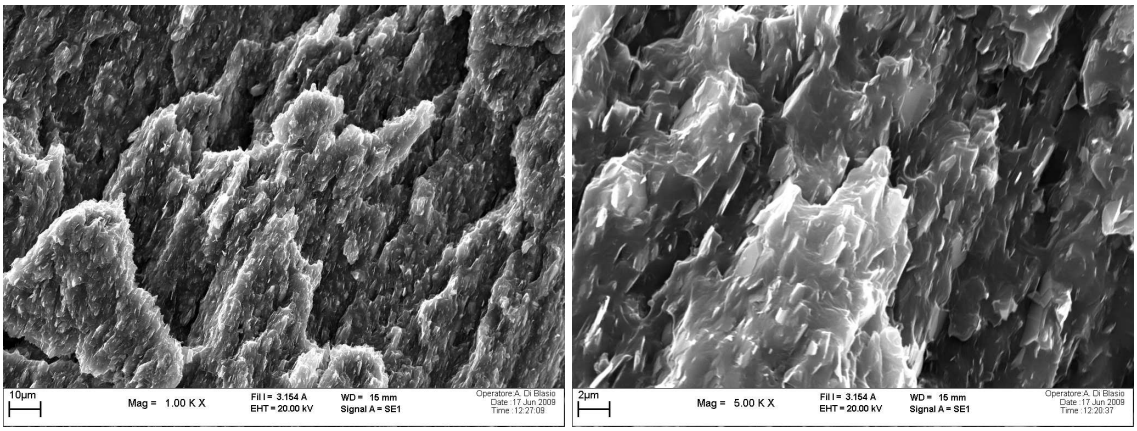

Figure 3: SEM micro-images of a sample with 30% (mass fraction) of graphite lamellae dispersed in a polypropylene matrix. Due to extrusion manufacturing, particles tend to align along a fixed axis (extrusion direction). The orizontal dimension of the image on the left-hand side is approximately $180\mu m$. The orizontal dimension of the image on the right-hand side is approximately $36\mu m$. Kindly provided by Dr A. Fina (Department of Materials Science and Chemical Engineering, Politecnico di Torino).

The scanning electron microscope (SEM) is the essential tool for performing micro-topology reconstruction. In organic polymers, which consist exclusively of light atoms such as carbon, hydrogen, oxygen, and nitrogen, the scattering is weak and therefore produces poor contrast. To meet these conditions needed for successful electron microscopy, polymers require special sample preparation. These obstacles can be combated and overcome by proper cleaning and drying, etching and staining of low contrast samples, lightly coating to prevent charging and protect from beam damage, making a pathway to ground with conductive paint or tape, and sectioning with an ultramicrotome for ultrathin sections [13].

Our modeling activity starts from SEM images of a composite material, obtained mixing polypropylene (PP) with the powder of a commercial graphite (KS4). Fig. 3 depicts the material sample along a fracture surface: Here, the one phase KS4 (brighter particles) is dispersed in the form of lamellae in a more abundant PP phase (darker part). Due to their significant anisotropy, during manufacturing, graphite particles tend to align along the extrusion axis, whose projection onto the image plane can be clearly distinguished in the micrographs of Fig. 3. As illustrated in the image on the left-hand side of Fig. 4, graphite particles will be represented by means of oblate ellipsoids, whose major axis $2a = 2b$, in the following, will be referred to as *particle size* ϕ.

Powders consist of a collection of particles, that can be characterized by a size distribution function. However, from product data-sheets, three values are typically assigned: D_{10}, D_{50}, D_{90} representing diameters at which 10%, 50% and 90% of powder particles have smaller size,

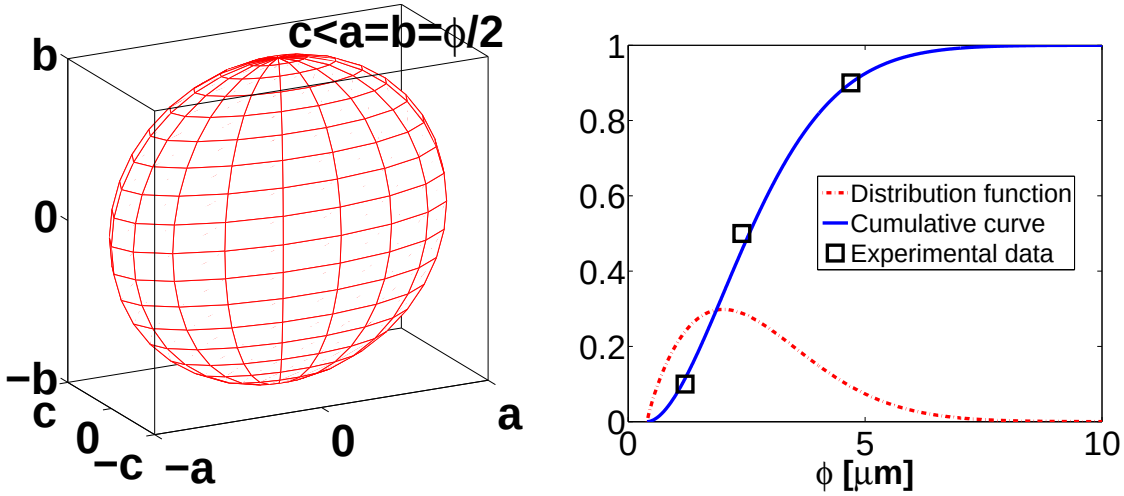

Figure 4: (Color online) Left-hand side: Graphite particles are modeled as oblate ellipsoids. Right-hand side: The ellipsoid size ϕ follows a distribution function (dashed line) reconstructed on the basis of cumulative experimental data (squares). The corresponding cumulative curve is also reported with a continuous line.

respectively. Therefore, the particle size distribution function $f(\phi)$ posses a cumulative curve

$$F(\phi) = \int_{\phi_{\min}}^{\phi} f(\varphi) d\varphi \tag{11}$$

matching those three points. The function f can be explicitly computed, as soon as more specific assumptions on its shape are made. In our simulations, we consider the following Poisson-like distribution function (which is suitable for characterizing small occurrences):

$$f(\phi') = \bar{\beta} \phi'^{\bar{\alpha}} e^{-[(\phi' - \bar{\mu})/\bar{\sigma}]^2}, \tag{12}$$

where the shift $\phi' = \phi - \phi_{min}$ imposes that no particle, with a size smaller than $\phi_{min} = 0.4\mu m$, is present. Other parameters $\bar{\beta}$, $\bar{\alpha}$, $\bar{\mu}$ and $\bar{\sigma}$ are free to choose under the condition that the corresponding cumulative curve is in agreement with the experimental data: D_{10}, D_{50}, D_{90}. On the right-hand side of Fig. 4, we show both the particle size distribution function f (computed according to (12)) and the cumulative curve corresponding to the KS4 graphite powder utilized in the material sample under study. Here, a good matching is achieved with the following choice of parameters:

$$\bar{\beta} = 0.51, \quad \bar{\alpha} = 0.87, \quad \bar{\mu} = -1.9, \quad \bar{\sigma} = 3.6. \tag{13}$$

The complete geometric characterization of the ellipsoid in Fig. 4 is accomplished as soon as it is known the minor axis $2c$, representing the thickness of the graphite platelets. To this respect, no experimental data were found, hence we must rely upon SEM micrographs such as the one reported in Fig. 3: Based on this kind of information, we can assume that platelet thickness is ranging from $2c \simeq 0.1\mu m$ up to $2c \simeq 0.3\mu m$. Below, in order to reduce the

computational cost, all simulations are performed with a fixed thickness $2c = 0.3\mu m$.

In the same spirit of the continuum percolation theory, the micro-topology of composite material samples is reconstructed by placing several oblate ellipsoids in a cube with the edge $L = 15\mu m$, following the methodology described below. We first generate an ellipsoid $\mathcal{E}$ centered at the origin $(x_0 = 0, y_0 = 0, z_0 = 0)$, and described by the equation:

$$\frac{x^2 + z^2}{a^2} + \frac{y^2}{c^2} = 1, \tag{14}$$

where $2a = \phi$ is a random value chosen from the distribution function in Fig. 4. Second, a linear transformation, describing a rigid rotation and translation, is imposed as follows:

$$\begin{bmatrix} x' \\ y' \\ z' \end{bmatrix} = R^{-1} \begin{bmatrix} x \\ y \\ z \end{bmatrix} + \begin{bmatrix} x_c \\ y_c \\ z_c \end{bmatrix}, \tag{15}$$

where the matrix $R = R_z R_y R_x$, with

$$R_x = \begin{bmatrix} 1 & 0 & 0 \\ 0 & \cos\vartheta_x & -\sin\vartheta_x \\ 0 & \sin\vartheta_x & \cos\vartheta_x \end{bmatrix}, R_y = \begin{bmatrix} \cos\vartheta_y & 0 & -\sin\vartheta_y \\ 0 & 1 & 0 \\ \sin\vartheta_y & 0 & \cos\vartheta_y \end{bmatrix}, R_z = \begin{bmatrix} \cos\vartheta_z & -\sin\vartheta_z & 0 \\ \sin\vartheta_z & \cos\vartheta_z & 0 \\ 0 & 0 & 1 \end{bmatrix}. \tag{16}$$

Here, (x_c, y_c, z_c) represent random coordinates of the center, while ϑ_x, ϑ_y and ϑ_z are the rotation angles around the x, y and z axes, respectively. In order to mimic the alignment of particles along a fixed extrusion axis, ϑ_z is chosen fully random, while ϑ_x and ϑ_y follow a Gaussian distribution around their mean values $\bar{\vartheta}_x$, $\bar{\vartheta}_y$ with a variance σ. Let us consider a $N \times N \times N$ regular Cartesian mesh where the edge of the cube $L = (N-1)dx$, with $dx = dy = dz$ denoting the spatial stepping. The mesh can be stored in a three dimensional array $\mathcal{M}$, where the presence of polymer matrix is denoted by $\mathcal{M}(i, \gamma, \tau) = 0$, while the filler by $\mathcal{M}(i, \gamma, \tau) = 1$. In the latter case, mesh nodes posses coordinates $\left(x'_f, y'_f, z'_f\right)$ that satisfy the following inequality:

$$\frac{x^2 + z^2}{a^2} + \frac{y^2}{c^2} \leq 1, \tag{17}$$

with

$$R \begin{bmatrix} x'_f - x_c \\ y'_f - y_c \\ z'_f - z_c \end{bmatrix} = \begin{bmatrix} x \\ y \\ z \end{bmatrix}. \tag{18}$$

Notice that, according to the formula (5), an arbitrary material sample with a prescribed volume fraction $\bar{p}_f$ is obtained by iterating the above construction subject to the following condition

$$1 - e^{-V_c} \leq \bar{p}_f, \tag{19}$$

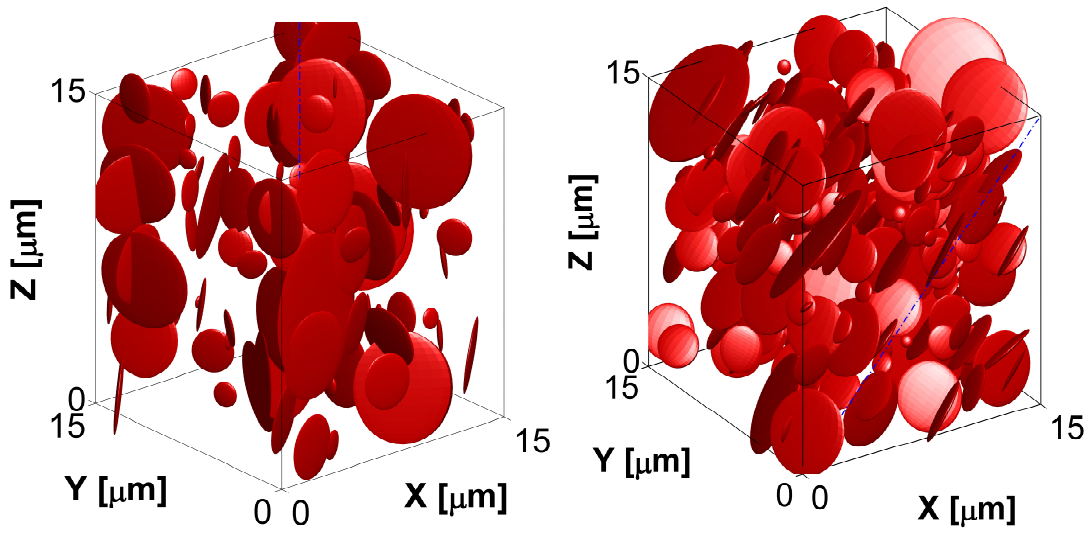

Figure 5: (Color online) Left-hand side: Reconstructions of three dimensional mixture of polypropylene (90% mass fraction) and graphite lamellae (10% mass fraction), where the extrusion axis is assumed parallel to z: $\bar{\vartheta}_x = \bar{\vartheta}_y = \bar{\vartheta}_z = 0$. Right-hand side: Reconstructions of three dimensional mixture of polypropylene (80% mass fraction) and graphite lamellae (20% mass fraction), where the extrusion axis is trasversal to z: $\bar{\vartheta}_x = \bar{\vartheta}_z = 0$, $\bar{\vartheta}_y = \pi/4$. Values $\rho_{PP} = 0.8903\,[g/cm^3]$ and $\rho_{KS4} = 2.255\,[g/cm^3]$ are adopted for the density of polypropylene and graphite, respectively.

where V_c represents the cumulative volume of the particles located within the unit box of Fig. 5.

In the latter figure, we show two examples of micro-topology reconstruction, where 10% mass fraction of graphite with $\bar{\vartheta}_x = \bar{\vartheta}_y = \bar{\vartheta}_z = 0$ and $\sigma = 0.15$ (left-hand side) are imposed. On the right-hand side of Fig. 5, we use 30% mass fraction of graphite with $\bar{\vartheta}_x = \bar{\vartheta}_z = 0$, $\bar{\vartheta}_y = \pi/4$ and $\sigma = 0.15$.

5. Mathematical model

By referring to the Fig. 5, at the steady state, we define the global thermal conductivity k_{eff} of a cubic sample of composite material by means of the following Fourier-like expression:

$$Q = -k_{eff} L L \frac{T_h - T_c}{L} = -k_{eff} L \left(T_h - T_c\right), \tag{20}$$

where the rate of conductive heat Q flows along the z-axis under a fixed temperature difference $(T_h - T_c)$ maintained between the uppermost facet (in the following, facet $\mathcal{A}$ at T_h) and the lowermost one (facet $\mathcal{B}$ at T_c). Let the above domain be discretized by a $(N \times N \times N)$ regular lattice with $dx = dy = dz$, such that $L = (N-1)\,dz$ with dx, dy and dz being the spacing along the x-, y- and z-axis respectively. The rate of heat Q through an arbitrary cross-section $\mathcal{S}$ (orthogonal to the z-axis), evaluated according to the Fourier's law, can be approximated as

follows:

$$Q = \int_{\mathcal{S}} -k\partial_z T d\mathcal{S} = \left| \sum_{i=1}^{(N-1)^2} \left(-k\partial_z T\right)_i dz^2 \right|_{\mathcal{S}} = \frac{L^2}{(N-1)^2} \left| \sum_{i=1}^{(N-1)^2} \left(-k\partial_z T\right)_i \right|_{\mathcal{S}}, \qquad (21)$$

where T and $\partial_z T$ denote the local temperature and the component of the temperature gradient along z, respectively, whereas the Fourier heat flux $\left(-k\partial_z T\right)_i$ is averaged over the four corners of the i-th computational cell. Moreover, the temperature difference between the facets $\mathcal{A}$ and $\mathcal{B}$ can be evaluated as follows:

$$(T_h - T_c) = \int_l \partial_z T dl,$$

where l is any continuous line connecting two arbitrary points of $\mathcal{A}$ and $\mathcal{B}$, respectively. In the following, for the sake of simplicity, we assume l parallel to the z-axis, hence:

$$(T_h - T_c) = \frac{L}{N-1} \left| \sum_{i=1}^{N-1} \left(\partial_z T\right)_i \right|_l, \qquad (22)$$

where the derivative $\left(\partial_z T\right)_i$ is averaged over the extreme values of the i-th computational segment of l. Upon substitution of (22) and (21) in the above expression (20), the global conductivity reads:

$$k_{eff} = \frac{\left| \sum_{i=1}^{(N-1)^2} \left(k\partial_z T\right)_i \right|_{\mathcal{S}}}{(N-1) \left| \sum_{i=1}^{N-1} \left(\partial_z T\right)_i \right|_l}. \qquad (23)$$

In our computations, according to other works [9, 10], we make use of a lattice Boltzmann (LB) method for solving the energy transport equation through non-homogeneous materials, where the multiphase conjugate heat transfer effect is automatically taken into account. In the LB method, each conservation law is related to a microscopic quantity which is conserved exactly by the collision operator of an evolution equation, describing the dynamics of distribution functions moving with discretized velocities between the nodes of the computational grid [14]. The LB models for convection-diffusion [15, 16, 17] are constructed similarly to hydrodynamic models: They are based on a hydrodynamic-type isotropic equilibrium function but discard momentum conservation. A similarity of equilibrium functions enables to build the tracer transport directly with the population solutions obtained for flow equation. In the following three dimensional computations, 19 discretized velocities are used: hence, the adopted lattice is the so-called $D3Q19$. Essentially, the numerical code is based on 19 distribution functions (or populations) f_i, which move on the above regular lattice with the following

velocities $\vec{c}_i = (c_{ix}, c_{iy}, c_{iz})$:

$$\begin{array}{ll} (0,0,0) & i = 0 \\ (\pm 1,0,0) & i = 1,2 \\ (0,\pm 1,0) & i = 3,4 \\ (0,0,\pm 1) & i = 5,6 \\ (\pm 1,\pm 1,0) & i = 7,...,10 \\ (0,\pm 1,\pm 1) & i = 11,...,14 \\ (\pm 1,0,\pm 1) & i = 15,...,18. \end{array}$$

According to the LB algorithm [16], population dynamics is dictated by the following equations at any point $\boldsymbol{x}$ of the spacial domain and any time instant t:

$$\partial_t f_i(\boldsymbol{x},t) + c_{i\beta}\partial_\beta f_i(\boldsymbol{x},t) = \omega\left(f_i^{eq}(T) - f_i(\boldsymbol{x},t)\right), \quad i = 0,...,18, \tag{24}$$

where ∂_t and ∂_β represent the partial derivatives with respect to time and spacial direction β respectively, while Einstein summation convention is adopted for the repeated index β. The equilibrium distribution functions are assumed $f_i^{eq}(T) = w_i T$, where w_i represents a fixed weight associated with the i-th population f_i:

$$\begin{array}{ll} w_i = 1/3 & i = 0 \\ w_i = 1/18 & i = 1,...,6 \\ w_i = 1/36 & i = 7,...,18. \end{array} \tag{25}$$

The zeroth- and first-order moments of populations f_i are related to the dimensionless temperature T and its gradient ∇T, respectively, as follows:

$$T = \sum_{i=0}^{18} f_i, \quad \vec{j} = (j_x, j_y, j_z) = \sum_{i=0}^{18} f_i \vec{c}_i = -\frac{c_s^2}{\omega}\nabla T, \tag{26}$$

with $c_s^2 = 1/3$. In the macroscopic limit, the LB equations (24) mimic the following partial differential equation (PDE) [16]:

$$\partial_t T + \nabla \cdot \vec{j} = -\frac{c_s^2}{2}\nabla^2 T. \tag{27}$$

Upon substitution of the expressions (26) in the equation (27) (under the assumptions of homogeneous and isotropic materials with constant physical properties), the latter PDE takes the form of the unsteady equation for heat conduction:

$$\partial_t T = \nabla \cdot (\alpha \nabla T) = \alpha \nabla^2 T, \tag{28}$$

if the thermal diffusivity $\alpha = k/\rho c_p$ is linked to the relaxation frequency ω as follows:

$$\alpha = c_s^2 \left(\frac{1}{\omega} - \frac{1}{2} \right), \tag{29}$$

with k, ρ and c_p denoting constant thermal conductivity, density and specific heat capacity, respectively. Let ω_f and ω_p be the relaxation frequencies corresponding to the filler (KS4) and the matrix (PP), respectively. In our computations, we make use of the following discretized form of equations (24):

$$f_i \left(\boldsymbol{x} + \vec{c}_i dt, t + dt \right) = f_i \left(\boldsymbol{x}, dt \right) + \omega_\gamma \left(f_i^{eq} \left(T \right) - f_i \left(\boldsymbol{x}, t \right) \right), \quad i = 0, ..., 18, \quad \gamma = f, p, \tag{30}$$

where dt is the discrete time step, and ω is locally adjusted in order to take into account of spatial inhomogeneity (different phases). The previous algebraic updating rule together with some numerical boundary conditions for f_i define the LB algorithm. In this work, we use the so-called anti-bounce-back (ABB) rule [18] for imposing the temperature at both ends of the simulated sample

$$f_i \left(\boldsymbol{x}_B, t + dt \right) - f_i^{eq} \left(T_\gamma(\boldsymbol{x}_B) \right) = f_{BB(i)}^{eq} \left(T_\gamma(\boldsymbol{x}_B) \right) - f_{BB(i)} \left(\boldsymbol{x}_B, t \right), \quad \gamma = f, p, \tag{31}$$

where $\boldsymbol{x}_B$ means a generic point at the ends of the computational domain, T_γ is the temperature prescribed by the boundary condition, i identifies a generic incoming direction $\vec{c}_i$ with regards to the computational domain and finally $BB(i)$ identifies the corresponding bounce-back direction, namely $\vec{c}_{BB(i)} = -\vec{c}_i$.

Notice that, rigorously speaking, the equations (24) can only be applied to homogeneous and isotropic materials with constant physical properties. Hence, although the above equations (30) remain valid within each of the two phases of the composite material in Fig. 5 (under the assumptions of homogeneous and isotropic phases), in general they do not hold globally due to an inaccurate treatment of the interface between PP and KS4. In other words, the model (30) automatically imposes both the continuity of the temperature field at the boundary points between two different phases:

$$T_f = T_p \tag{32}$$

and the continuity of the flux of vector $\alpha \nabla T$ (it can be proven by applying the Gauss-Green theorem to Eq. (28)):

$$\left(\alpha_f \nabla T_f \cdot \hat{n} \right) / \left(\alpha_p \nabla T_p \cdot \hat{n} \right) = 1, \tag{33}$$

where the unity vector $\hat{n}$ is locally normal to the interface, while the subscripts f and p denote quantities which are evaluated within the filler and the matrix, respectively.

On the other hand, using (26) and (29), the Fourier heat flux can be recast as

$$\vec{q} = -k \nabla T = \rho c_p \left(1 - \frac{\omega}{2} \right) \vec{j}, \tag{34}$$

whereas the continuity of its normal component, at any interface, requires

$$\left(\vec{q}_f \cdot \hat{n}\right) / \left(\vec{q}_p \cdot \hat{n}\right) = 1, \tag{35}$$

or equivalently

$$\left(\alpha_f \nabla T_f \cdot \hat{n}\right) / \left(\alpha_p \nabla T_p \cdot \hat{n}\right) = \left(\rho c_p\right)_p / \left(\rho c_p\right)_f . \tag{36}$$

Hence, we note that the correct condition at the interface between two different phases (36) can be approximated by (33) only in the case:

$$\left(\rho c_p\right)_p \cong \left(\rho c_p\right)_f . \tag{37}$$

Nevertheless, it is worth stressing that, at the steady state, the equation for heat conduction (28) takes the simpler form:

$$k\nabla^2 T = 0, \tag{38}$$

where, according to (29), a constant k is linked to the relaxation frequency ω

$$k = c_s^2 \left(\frac{1}{\omega} - \frac{1}{2}\right), \tag{39}$$

and can be interpreted as thermal conductivity. We stress that, all values below are computed at the steady state, hence we do not need to resort to the approximation (37) and further make use of the relationship (39). Accordingly, at the steady state, the global thermal conductivity k_{eff} can be formulated by recasting the formula (23) as follows:

$$k_{eff} = \frac{\left|\sum_{i=1}^{(N-1)^2} \left(k\partial_z T\right)_i\right|_{\mathcal{S}}}{(N-1)\left|\sum_{i=1}^{N-1} \left(\partial_z T\right)_i\right|_l} = \frac{\left|\sum_{i=1}^{(N-1)^2} \left(-j_z + \frac{1}{2}\omega_\gamma j_z\right)_i\right|_{\mathcal{S}}}{(N-1)\left|\sum_{i=1}^{N-1} \left(-\frac{\omega_\gamma}{c_s^2} j_z\right)_i\right|_l}, \quad \gamma = f, p, \tag{40}$$

where, in evaluating the numerator of the latter expression, the relation given by Eq. (34) has been used. In all the simulations below, k_{eff} is computed by means of the expression (40), where the summation at the numerator is replaced with its averaged value over the N surfaces $\mathcal{S}_\tau$ with $0 < x, y < L$, $z = \tau dz$ and $\tau = 0, ..., N-1$. Similarly, the summation at the denominator of (40) is replaced by its averaged value over the N^2 vertical line segments $l_{i,\gamma}$ with $0 < z < L$, $x = idx$, $y = \gamma dy$ and $i, \gamma = 0, ..., N-1$. We stress that, all the quantities in (40) can be explicitly computed, and thus the suggested model makes no use of empirical factors. Eqs. (28) (written for both the filler and the polymer matrix), (32) and (36) describe a classical example of multiphase conjugate heat transfer problem. In this respect, the lattice Boltzmann method proves particularly efficient compared to conventional numerical methods (such as finite difference and finite element methods), where a tremendous computational effort is spent imposing the interface constraints [9].

Finally, all computations below are carried out by the LABORA code. The LABORA (LAttice

k_f/k_p	ω_1	ω_2	Deviation
19	0.1	1	13.9%
81	0.2	1.8	13.2%
199	0.01	1	56.9%
1800	0.0011	1	65.4%

Table 1: Thermal resistances in parallel with $p_f = 0.111$ are simulated at different ratios k_f/k_p. Results are compared to the corresponding theoretical values: The choice of the relaxation frequencies ω_γ significantly affects the accuracy of numerical predictions.

BOltzmann for Raster Applications) project started back in 2005 and it originally aimed at developing a 3D parallel code for simulating fluid flow of reactive mixtures through complex geometries [19]. In particular, the LABORA code was developed in C++ by extensive use of the object programming. In the first release, the free communication library MPICH 1.3 was adopted, while nowadays OPENMPI is used, both based on MPI technology [20].

Concerning the hardware, the reported numerical results were obtained by the EnerGRID computational facility, available at Politecnico di Torino (Italy). The EnerGRID computational facility consists of a Transtec(R) HPC cluster, made of 72 total virtual cores, with 144 GB of total RAM, 5.5 TB total disk capacity (3.0 TB failure free) and a double networking system (Infiniband for processing data and GBit for monitoring). The tested peak performance (according to the TOP500 standard [21]) is 376.09 GFlop/s with mvapich2/IB (which is roughly 60 of the theoretical peak performance 596.48 GFlop/s).

6. Code validation

The numerical model described in the above section 5 has been validated in the case of thermal resistances connected in series and in parallel arrangements. Specifically, by referring to the picture on the left-hand side of Fig. 1, the global thermal conductivity of such an ideal composite material can be computed along both the z-axis (parallel arrangement) and the x-axis (series arrangement), in order to compare the simulation results with the corresponding exact values:

$$k_{eff} = p_f k_f + (1 - p_f)\, k_p, \tag{41}$$

$$k_{eff} = \left[p_f \frac{1}{k_f} + (1 - p_f)\, \frac{1}{k_p} \right]^{-1}, \tag{42}$$

valid for resistances in parallel and in series, respectively. Validation results are reported in Fig. 6 in terms of the dimensionless ratio k_{eff}/k_p. Here, using 60^3 lattice nodes, deviations can be bounded up to a few percent by restricting the choice of the relaxation frequencies within the following range: $0.5 \leq \omega_f, \omega_p < 2$. On the contrary, as summarized in Table 1, remarkably larger deviations have been observed as soon as the lower limit of ω_γ is decreased further down: $\omega_\gamma \leq 0.2$. Notice that, the latter result is not surprising, since it is well known

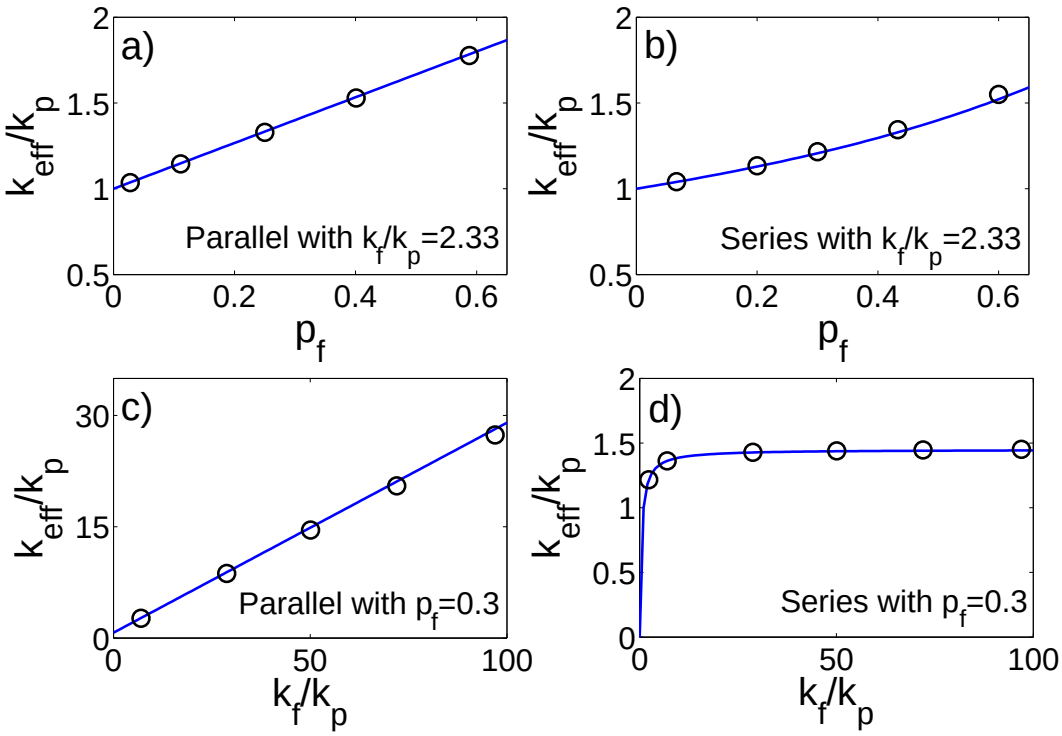

Figure 6: (Color online) Comparison between the simulation results (circles) and the exact values (continuous lines) of k_{eff}/k_p for thermal resistances placed in series and in parallel arrangements. a) Thermal resistances arranged in parallel with a fixed ratio $k_f/k_p = 2.33$ evaluated at several volume fractions p_f: The maximal deviation is 0.45%. b) Thermal resistances arranged in series with a fixed ratio $k_f/k_p = 2.33$ evaluated at several volume frations p_f: The maximal deviation is 1.7%. c) Thermal resistances arranged in parallel with a fixed volume fraction $p_f = 0.3$ at several ratios k_f/k_p: The maximal deviation is 2.5%. d) Thermal resistances arranged in series with a fixed volume fraction $p_f = 0.3$ at several ratios k_f/k_p: The maximal deviation is 0.6%.

	Y_f	k_{eff}/k_p along z-axis	k_{eff}/k_p along x-axis	Lattice nodes
S_1	0.298	3.21	2.24	120^3
S_2	0.295	3.20	2.17	120^3
S_3	0.297	3.24	2.40	120^3
S_4	0.303	3.35	2.28	120^3
S_5	0.302	3.16	2.24	120^3
S_6	0.297	3.22	2.18	120^3
S_7	0.299	3.23	2.20	120^3
S_8	0.295	3.20	2.29	120^3
S_9	0.300	3.36	2.33	120^3
S_{10}	0.302	3.32	2.26	120^3
Mean value	-	3.25	2.26	-
Variance	-	0.00505	0.00503	-
S_{11}	0.296	3.36	2.27	240^3

Table 2: Ten composite material samples have been generated with $Y_f = 0.3 \pm 0.005$: Ratios k_{eff}/k_p have been computed along both the z-axis and x-axis for any of the i-th sample S_i with a fixed ratio $k_f/k_p = 36.5$ using 120^3 lattice nodes.

that the accuracy of LBM in the parameter range $0 < \omega_\gamma < 1$ is much smaller than that in the the upper range $1 \leq \omega_\gamma < 2$ (see Fig. 5 in Ref. [22]).

7. Numerical results

In the following, we investigate the dependence of the global thermal conductivity k_{eff} on the values k_f, k_p and orientation of the extrusion axis, in composite material samples with a fixed amount of filler. First of all, toward the end of verifying the repeatability of the reconstruction strategy described in section 4, ten different random samples $S_{i=1,\dots,10}$ are generated by setting $Y_f = 0.3 \pm 0.005$, $L = 15\mu m$, $k_f/k_p = 36.5$, and imposing the extrusion axis parallel to z: $\bar{\vartheta}_x = \bar{\vartheta}_y = \bar{\vartheta}_z = 0$ with $\sigma = 0.15$. Any of the latter micro-topology is discretized by means of a regular lattice with 120^3 nodes, whereas the ratio k_{eff}/k_p is computed along both the z- and x-axis: As reported in Table 2, results fluctuate around a mean value with variance ≈ 0.005. Notice that, grid-independence of the above numerical predictions is demonstrated by consistent simulation results of one more sample S_{11} discretized by means of 240^3 lattice nodes. Furthermore, various computations have been carried out adopting the reconstruction S_1 ($Y_f = 0.298$) in correspondence of different values k_f/k_p: Results are illustrated in Fig. 7 along with the corresponding theoretical solutions for thermal resistances in parallel and series arrangements, as dictated by formula (41) and (42), respectively. Numerical evidences suggest a remarkable linear dependence of k_{eff}/k_p starting from $k_f/k_p \approx 45 - 50$. In particular, the tendency lines in the picture on the left-hand side of Fig. 7 are evaluated by the least squares method, on the basis of data with $k_f/k_p > 40$, and the following coefficients of determination are found: $R_z^2 = 0.997$, $R_x^2 = 0.975$ for the results along the z-axis and x-axis, respectively. Notice that, the latter feature proves particularly convenient in the case of phases with large

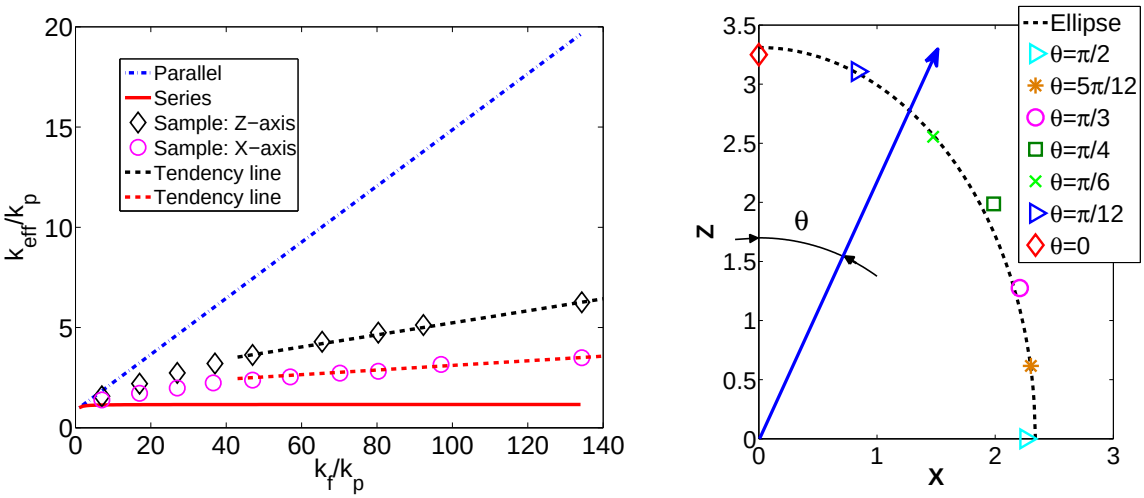

Figure 7: (Color online) Left-hand side: Simulation results of a material sample with $Y_f = 0.298$ at different ratios k_f/k_p. Ratios k_{eff}/k_p have been evaluated along both the $z-$axis (diamonds) and the $x-$axis (circles). Starting from $k_f/k_p \approx 50$ a linear dependence can be observed. Right-hand side: Polar diagram of the ratio k_{eff}/k_p. Several material samples are reconstructed under fixed mass fraction $Y_f = 0.3 \pm 0.005$ and different orientations of the extrusion axis (thick arrow). Simulation results (symbols), under fixed conductivity ratio $k_f/k_p = 36.5$, tend to be located along an *ellipse of thermal conductivity* (dashed line), typically observed in anisotropic materials.

conductivity ratios (e.g., $k_f/k_p > 100$) where, in order to avoid both significant numerical errors ($\omega_\gamma < 0.2$) and prohibitively long computations ($\omega_\gamma \approx 2$), the value k_{eff}/k_p can be linearly extrapolated from results obtained at lower ratios (e.g., $60 < k_f/k_p < 80$). Finally, in order to investigate the dependence of k_{eff}/k_p on the orientation of the extrusion axis, composite material samples have been reconstructed imposing: $Y_f = 0.3 \pm 0.005$, $\bar{\vartheta}_x = \bar{\vartheta}_z = 0$, $\bar{\vartheta}_y = \theta$, and $k_f/k_p = 36.5$. Results are shown by means of a polar diagram on the right-hand side of Fig. 7 for different values of θ, and a typical *ellipse of thermal conductivity* of highly anisotropic materials is shown. Notice that, anisotropy of thermal conductivity typically arises from experiments on composite materials, and the ellipse of thermal conductivity can be observed by using, for instance, photoreflectance microscopy (see, e.g., [23]). Each configuration $S_{i=1,\ldots,10}$ reported in Table 2 and in Fig. 7, was computed by using 64 processors on the EnerGRID computational facility, where 100000 LB steps require ≈ 6 hours to be completed.

8. Discussion and outlook

In this paper, we illustrate a general methodology for both accurately reconstructing the micro-topology of composite materials, and predicting the global thermal conductivity k_{eff}, by means of the lattice Boltzmann method, which has revealed suitable for handling such complex geometries [16]. More specifically, here the dependence of k_{eff} on the thermal conductivity k_p of a polymer matrix (polypropylene) and the thermal conductivity k_f of a filler compound (graphite particles) is investigated at a fixed content of graphite. In this respect, a remarkable linear dependence of k_{eff}/k_p on the ratio k_f/k_p, starting from $k_f/k_p \approx 45 - 50$,

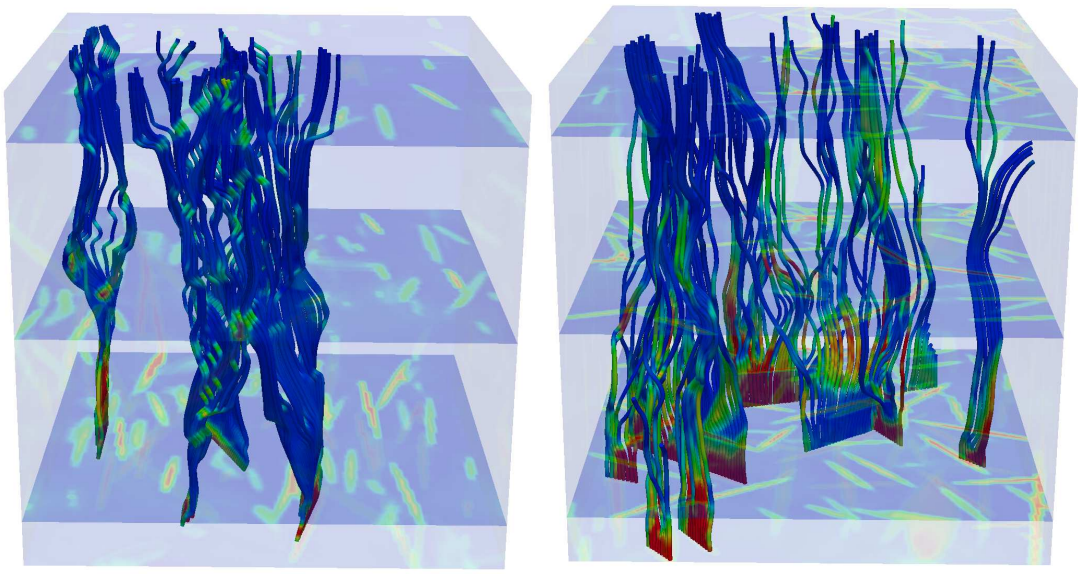

Figure 8: (Color online) $Y_f = 0.298$, $k_f/k_p = 36.5$. Left-hand side: Streamlines of the heat flux along percolating paths, where the extrusion axis is aligned with the $x-$axis. Right-hand side: Streamlines of the heat flux along percolating paths, where the extrusion axis is aligned with the $z-$axis. Colors provide an indication of the heat flux intensity.

is observed. Such an evidence suggests an indirect method for computing the global thermal conductivity corresponding to phases with large conductivity ratios (e.g., $k_f/k_p > 100$), where it becomes desirable to avoid both significant numerical errors ($\omega_\gamma < 0.2$) and long computations ($\omega_\gamma \approx 2$). Moreover, the anisotropy of the k_{eff} in such a composite material is demonstrated by computing the ellipse of thermal conductivity, consistently also with experimental evidences [23]. Finally, it is worth stressing that the numerical tool described in this work may be utilized, in combination with experimental data, for characterizing the contact between filler particles in a percolating path. Here, any percolating cluster of filler particles is considered homogeneous and isotropic, so that thermal conductivity can be described by a constant value k_f. However, more rigorously, at the interface between filler particles, the effects due to interfacial thermal resistances and weak contact are to be considered since they do play an important role in heat conduction (see, e.g., [24, 25, 26]). Hence, k_f is to be interpreted as an *effective thermal conductivity* of the filler within percolating paths, rather than thermal conductivity of pure filler k_f^p. In other words, comparing the numerical prediction for k_{eff} with the corresponding experimental data, it is possible to estimate a deviation of the effective thermal conductivity k_f from k_f^p, which globally quantifies the above effects. However, it worth noticing that investigations on the mechanism behind heat flow phenomena at the interface filler-particle and particle-particle have revealed quite challenging so far, and many issues are still open [24, 27]. Hence, there is a demand for more detailed studies on heat transfer across different phases, and the presented modeling activity will proceed further along that direction in the near future: In this respect, we note that lattice Boltzmann schemes for modeling contact resistances have been recently suggested in the literature (see, e.g., [28]).

9. Acknowledgments

The research leading to these results has received funding from the European Community's Seventh Framework Programme (FP7 2007-2013) under grant agreement N. 227407 - Thermonano. We are indebted to Prof. Guido Saracco and Dr. Alberto Fina for proving us with SEM micro-images and for the useful discussions. Prof. Michele Cali and Prof. Romano Borchiellini are gratefully acknowledged for supporting this work. We wish to state our appreciation to Valerio Novaresio for the precious help in obtaining the images in Fig. 8. Finally, useful discussions are acknowledged with Dr. Ahmad Al-Zoubi, Prof. Dimosthenis Trimis and Prof. Ulrich Gross of Technical University Berg-akademie Freiberg (TUBAF).

References

[1] D. Stauffer, and A. Aharony, Introduction to Percolation Theory, second ed., Taylor & Francis, London, (1994), pp. 89–103.

[2] G. E. Pike, and C. H. Seager, Percolation and conductivity: A computer study. I, Phys. Rev. B 10 (1974) 1421–1434.

[3] Y. B. Yi, and A. M. Sastry, Analytical approximation of the two–dimensional percolation threshold for fields of overlapping ellipses, Phys. Rev. E 66 (2002) 066130.

[4] W. Xia, and M. F. Thorpe, Percolation properties of random ellipses, Phys. Rev. A 38 (1988) 2650–2656.

[5] L. Berhan, Y. B. Yi, A. M. Sastry, E. Munoz, M. Selvidge, and R. Baughman, Mechanical properties of nanotube sheets: Alterations in joint morphology and achievable moduli in manufacturable materials, J. App. Phys. 95 (2004) 4335–4345.

[6] L. Berhan, and A. M. Sastry, Modeling percolation in high–aspect–ratio fiber systems. I. Soft–core versus hard–core models, Phys. Rev. E 75 (2007) 041120.

[7] L. Berhan, and A. M. Sastry, Modeling percolation in high–aspect–ratio fiber systems. II. The effect of waviness on the percolation onset, Phys. Rev. E 75 (2007) 041121.

[8] Y. B. Yi, and E. Tawerghi, Geometric percolation thresholds of interpenetrating plates in three–dimensional space, Phys. Rev. E 79 (2009) 041134.

[9] J. Wang, M. Wang, and Z. Li, A lattice Boltzmann algorithm for fluid-solid conjugate heat transfer. International Journal of Thermal Sciences 46 (2007) 228–234.

[10] M. Wang, J. He, J. Yu, and N. Pan, Lattice Boltzmann modeling of the effective thermal conductivity for fibrous materials. International Journal of Thermal Sciences 46 (2007) 848–855.

[11] E. J. Garboczi, K. A. Snyder, J. F. Douglas, and M. F. Thorpe, Geometrical percolation threshold of overlapping ellipsoids, Phys. Rev. E 52 (1995) 819–828.

[12] Y. B. Yi, and A. M. Sastry, Analytical approximation of the percolation threshold for overlapping ellipsoids of revolution, Proc. R. Soc. London, Ser. A, 460 (2004) 2353–2380.

[13] A.M. Schrand, Polymer Sample Preparation for Electron Microscopy, Advances in Instrumentation and Techniques – Metallographic Techniques and Applications, Microscopy and Microanalysis 2005 in Honolulu, Hawaii, USA, July 31–August 4, 2005.

[14] I. Ginzburg, Equilibrium–type and Link–type Lattice Boltzmann models for generic advection and anisotropic–dispersion equation. Adv. Water Resour. 28 (2005) 1171–1195.

[15] E. G. Flekkoy, U. Oxaal, J. Feder, T. Jossang, Hydrodynamic dispersion at stagnation points–simulations and experiments, Phys Rev E 52 (1995) 4952–4962.

[16] D. Wolf-Gladrow, Lattice gas cellular automata and lattice Boltzmann models: an introduction, Lecture notes in mathematics, vol. 1725, Springer, (2000).

[17] R. G. M. Van der Sman, M. H. Ernst, Advection–diffusion lattice Boltzmann scheme for irregular lattices, J. Comp. Phys. 160 (2000) 766–782.

[18] I. Ginzburg, Generic boundary conditions for Lattice Boltzmann models and their application to advection and anisotropic-dispersion equations. Adv. Water Resour. 28 (2005) 1196–1216.

[19] P. Asinari, M. Cali, M.R. von Spakovsky, and B.V. Kasula, Direct numerical calculation of the kinematic tortuosity of reactive mixture flow in the anode layer of solid oxide fuel cells by the lattice Boltzmann method, Journal of Power Sources 170 (2007) 359–375.

[20] Writing Message–Passing Parallel Programs with MPI, Edinburgh Parallel Computing Centre, The University of Edinburgh.

[21] http://www.top500.org/

[22] P. Asinari, T. Ohwada, Connection between kinetic methods for fluid–dynamic equations and macroscopic finite–difference schemes, Computers and Mathematics with Applications, 58 (2009) 841–861.

[23] D. Rochais, H. Le Houëdec, F. Enguehard, J. Jumel, and F. Lepoutre, Microscale thermal characterization at temperatures up to 1000C by photoreflectance microscopy. Application to the characterization of carbon fibres, J. Phys. D: Appl. Phys. 38 (2005) 1498–1503.

[24] S.T. Huxtable, D.G. Cahill, S. Shenogin, L. Xue, R. Ozisik, P. Barone, M. Usrey, M.S. Strano, G. Siddons, M. Shim, and P. Keblinski, Interfacial heat flow in carbon nanotube suspensions. Nature Materials 2 (2003) 731–734.

[25] S. Shenogin, L. Xue, R. Ozisik, P. Keblinski, and D.G. Cahill, Role of thermal boundary resistance on the heat flow in carbon–nanotube composites. J Appl Phys 95 (2004) 8136–8144.

[26] I.V. Singh, M. Tananka, and M. Endo, Effect of interface on the thermal conductivity of carbon nanotube composites. International Journal of Thermal Sciences 46 (2007) 842–847.

[27] T. Chen, G.J. Weng, and W.C. Liu, Effect of Kapitza contact and consideration of tube-end transport on the effective conductivity in nanotube-based composites. J. Appl. Phys. 97 (2005) 104312.

[28] K. Han, Y.T. Feng, and D.R.J. Owen, Modelling of thermal contact resistance within the framework of the thermal lattice Boltzmann method. International Journal of Thermal Sciences 47 (2008) 1276–1283.